Exp Fluids (2009) 46:285–296
DOI 10.1007/s00348-008-0559-4

RESEARCH ARTICLE

Three-dimensional magnetic resonance velocimetry measurements of turbulence quantities in complex flow

Christopher J. Elkins · Marcus T. Alley · Lars Saetran · John K. Eaton

Received: 15 February 2007 / Revised: 21 August 2008 / Accepted: 22 August 2008 / Published online: 13 September 2008

Abstract A magnetic resonance velocimetry (MRV) experimental technique based on magnetic resonance imaging and capable of measuring the turbulent Reynolds stresses in a 3D flow domain is described. Results are presented in backward facing step flow in a square channel with a Reynolds number of 48,000 based on step height and freestream velocity at the step. MRV results are compared to particle image velocimetry (PIV) measurements in the centerplane containing the streamwise and cross-stream axes. MRV and PIV mean velocity measurements show excellent agreement. MRV measurements for Reynolds normal stresses compare to within ±20% of the PIV results while results for the turbulent shear are less accurate.

1 Introduction

The design of fluid passages in modern engineering devices requires detailed understanding of highly complex 3D turbulent flow. Engineers rely heavily on computational fluid dynamics (CFD) to predict the flow behavior. However, CFD requires experimental confirmation in these complex flows, especially when the flows include regions of separation and recirculation. There is a real need for an experimental technique capable of providing 3D full field velocity measurements that are comparable to CFD results. Magnetic resonance velocimetry (MRV) is a non-invasive technique capable of producing detailed full field mean velocity measurements in highly complex turbulent flows in and around opaque objects (general reference: Caprihan and Fukushima 1990; specific to complex flow models: Elkins et al. 2003, 2004). Using rapid prototype manufacturing, complex flow passages can be manufactured precisely as they are drawn in CAD software. MRV measurements can be made in the same geometry used for CFD simulations, and the results from both methods are easily compared (Iaccarino and Elkins 2006). An advantage of MRV is that experiments detailing the entire 3D flow field can be performed in a few hours. To date, the MRV and CFD complement each other well since the MRV provides an experimental check for the mean velocities in the CFD results, while the CFD provides details about the turbulent velocity fluctuations, turbulent shear stresses, wall shear stress, pressure, etc. In some cases, it is the turbulence properties themselves that are of most interest. Ideally, these turbulence quantities could be measured using MR techniques as well, and this paper details our efforts to extend MRV methods to measure the turbulent normal and shear stresses in complex 3D flows.

Past developments in magnetic resonance techniques for measuring turbulent velocity variances have focused primarily on 2D cross sections of turbulent pipe flow (Gao and Gore 1991; Li et al. 1994; Gatenby and Gore 1996) and stenotic (partially obstructed) pipes (Gatenby and Gore 1994; Dyverfeldt et al. 2006) because of the relevance to physiological flow through blood vessels. Newling et al. (2004) measured the turbulent kinetic energy in the flow of

C. J. Elkins (✉) · J. K. Eaton
Mechanical Engineering Department, Stanford University, Bldg. 500, Stanford, CA 94305, USA
e-mail: celkins@stanford.edu

M. T. Alley
Department of Radiology, Lucas MRI/S Center, Stanford University, Stanford, CA 94305, USA

L. Saetran
Department of Energy and Process Engineering, Norwegian University of Science and Technology, 7491 Trondheim, Norway

gaseous SF_6 over an abrupt step obstruction in a pipe with a bulk mean velocity of 17 m/s.

Many studies (De Gennes 1969; Kuethe 1989; Gao and Gore 1991; Gatenby and Gore 1994; Kuethe and Gao 1995; Newling et al. 2004; Dyverfeldt et al. 2006) used methods based on diffusion principles in which turbulence causes a loss of the net magnetization through a process known as intravoxel phase dispersion. Spins having different velocities within a voxel have correspondingly different phases which add incoherently, thus reducing the overall signal in the final image. These studies derived relationships to predict the turbulent velocity statistics from the measured amount of signal loss. The derivations are based on assumptions about the turbulence characteristics, such as homogeneity and isotropy, and Lagrangian or Eulerian turbulent correlation times, depending on the derivation.

Kuethe and Gao (1995) evaluated several of these analyses in fully developed turbulent pipe flow for a large range of magnetic field gradient amplitudes and timing parameters. They found the derivations of Gao and Gore (1991) and Kuethe (1989) produce satisfactory estimates for the signal loss due to turbulence in pipe flow. They also found that knowledge of the turbulent correlation times is necessary for accurate predictions unless the measurement times and turbulent correlation times differ by a factor of 10. Asymptotic results based on assumptions of very long or very short correlation times relative to the measurement time can be used in such cases. They also point out that the assumption of homogeneous turbulence can produce significant errors in regions of the flow where homogeneity is a bad assumption.

In this paper, we apply the method of Gao and Gore (1991) to provide full-field 3D measurements of the turbulent Reynolds stresses. Their derivation is modified to account for non-idealized bipolar gradients (see Fig. 1) implemented in a clinical 1.5-T MR system (GE Signa CV/I, $G_{max} = 50$ mT/m, rise time $= 268$ μs) in which magnetic field gradients are applied for short times on the order of 1 ms with amplitudes as high as 5 G/cm. These imaging sequence parameters are necessary for short total scan times to acquire a 3D image while at the same time producing measurable signal loss from turbulence.

The objective of this paper is to evaluate a 3D imaging sequence and method for measuring turbulence statistics and shear stresses. The method is evaluated by taking MR measurements in the flow downstream of a backward facing step in a square channel and directly comparing them to particle image velocimetry (PIV) measurements in the same flow. The backward facing step flow affords quantitative characterization of the MRV results in the presence of a growing shear layer with variable mean shear rates, a large range of turbulent stress levels, and a large range of turbulent correlation times.

2 Materials and methods

2.1 MR system and sequence

Hydrogen nuclei in a strong magnetic field, $\vec{B}$, align their spins with the direction of the field, typically defined as the z-direction. Radio frequency (RF) pulses at the resonant or Larmor frequency, $\omega_0 = \gamma|\vec{B}|/2\pi$, cause these nuclei to orient their spins perpendicular to the main magnetic field direction thereby obtaining "transverse magnetization". Here, γ is the nuclear gyromagnetic ratio. After the termination of the RF pulse, the spins precess at the local Larmor frequency about an axis parallel to the z-direction while they recover their longitudinal component. The time-varying fields that result from the precession of the spins induce voltages in nearby receiver coils which are then detected by the MR system.

Using spatial magnetic field gradients, spin location and motion can be encoded in the frequency and phase of the measured signals. By applying a bipolar magnetic field gradient (see Fig. 1) in addition to imaging gradients, an image of fluid motion can be created in which the phase of the signal $S(t)$ in each voxel is a measure of the mean velocity of the fluid at that location. The method for measuring the mean flow based on the signal phase is called phase contrast MRI (PC-MRI). When the flow is turbulent, the randomness of the fluid motion causes phase dispersion and attenuation in the signal magnitude $|S(t)|$, henceforth denoted by S, which can be related to the variance of the velocity.

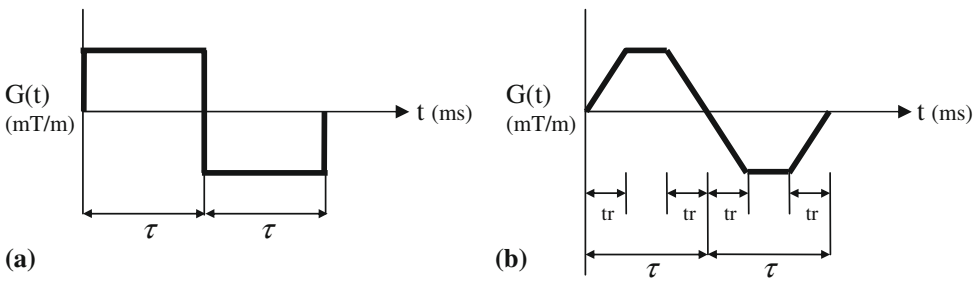

Fig. 1 **a** Idealized bipolar gradient with single lobe duration τ and amplitudes $\pm G$. **b** Bipolar gradient applied in this experiment with ramp time tr, single lobe duration τ, and time varying amplitude $G(t)$

Following the derivation of Gao and Gore (1991) for the bipolar gradients used in this experiment and illustrated in Fig. 1b, the signal magnitude for an image voxel is an ensemble average of the signal from many fluid elements and given by

$$S \equiv \langle S(t) \rangle = S_0 e^{-\gamma^2 G^2 \langle u'^2 \rangle f(\tau, \mathrm{tr}, T_0)} \quad (1)$$

where S_0 is the signal without phase dispersion, G is the maximum amplitude of the bipolar gradient, u' is the fluctuating velocity, $\langle u'^2 \rangle$ is the variance of the velocity, and $f(\tau, \mathrm{tr}, T_0)$ is a timing function given by

$$f(\tau, \mathrm{tr}, T_0) = \frac{T_0 \left(\begin{array}{r} 30T_0^5 e^{2\tau/T_0} + 60T_0^5 e^{3\mathrm{tr}/T_0}\left(-1 + e^{\tau/T_0}\right) + 60T_0^5 e^{(\tau+\mathrm{tr})/T_0}\left(-1 + e^{\tau/T_0}\right) - 30T_0^5 e^{4\mathrm{tr}/T_0}\left(-1 + 2e^{\tau/T_0}\right) \\ + e^{2\mathrm{tr}/T_0}\left(30T_0^5 + 60T_0^5 e^{\tau/T_0} - e^{2\tau/T_0}\left(\begin{array}{r} 90T_0^5 - 120\mathrm{tr}T_0^4 + 20\mathrm{tr}^2 T_0^2 (3\tau - 4\mathrm{tr}) \\ + \mathrm{tr}^2\left(-20\tau^3 + 30\mathrm{tr}\tau^2 + 5\mathrm{tr}^2\tau - 16\mathrm{tr}^3\right) \end{array}\right)\right) \end{array} \right)}{\left(30\mathrm{tr}^2 e^{2(\tau+\mathrm{tr})/T_0}\right)} \quad (2)$$

The bipolar gradients used in this study have a single lobe duration, τ, that is 740 μs, and a ramp time, tr, of 336 μs. The turbulence is assumed to be a random process that is homogeneous, statistically stationary, and ergodic with Gaussian velocity distributions.

The derivation of Gao and Gore is based on the commonly used model for the Lagrangian autocorrelation function,

$$R_L(t) \equiv \langle u'(t)u'(t+t') \rangle / \langle u'^2 \rangle = e^{-|t|/T_0} \quad (3)$$

in which the timing parameter T_0 is the Lagrangian integral time scale. Strictly speaking, this common model is not accurate for short times when $R_L(t) = 1$ and long times when the autocorrelation can become negative in some flows.

Figure 2 shows $f(\tau, \mathrm{tr}, T_0)$ plotted against values of T_0 for the bipolar gradient timing used in this experiment. A value for T_0 is required in order to calculate $f(\tau, \mathrm{tr}, T_0)$, but T_0 is unknown and typically spatially dependent. However, as Fig. 2 shows, $f(\tau, \mathrm{tr}, T_0)$ grows quickly to an asymptotic value when T_0 is greater than a few ms. An equation for the asymptotic value for large T_0 can be derived by Taylor expanding Eq. 2, discarding the terms with exponents higher than 5th order, and neglecting the terms with T_0 in the denominator. This produces the equation

$$f(\tau, \mathrm{tr}, T_0) = \frac{1}{2}\mathrm{tr}^2\tau^2 - \mathrm{tr}\tau^3 + \frac{1}{2}\tau^4 \quad (4)$$

valid when $T_0 \gg \tau$. The asymptotic value for $f(\tau, \mathrm{tr}, T_0)$ applies with at least 92% accuracy to parts of the flow with integral time scales larger than 3 ms. The topic of determining local values for $f(\tau, \mathrm{tr}, T_0)$ is continued in Sect. 4.

The form of Eq. 1 indicates that MR signal loss increases with increasing bipolar gradient amplitude, duration of the bipolar gradient, and turbulent velocity variance. Rearranging Eq. 1 gives an equation for the velocity variance,

$$\sigma_u^2 = \langle u'^2 \rangle = \frac{\ln(S_0/S)}{\gamma^2 G^2 f(\tau, \mathrm{tr}, T_0)} \quad (5)$$

Following Gao and Gore, several images of the flow can be made by varying the amplitude and timing of the bipolar gradient, and the velocity variance for each voxel in the flow can be calculated from a least squares fit of $\ln(S_0/S)$ versus $\gamma^2 G^2 f(\tau, \mathrm{tr}, T_0)$. In the present experiment, the baseline S_0 values are obtained using the imaging gradients shown in Fig. 3, but with zero amplitude bipolar gradients ($G = 0$). The S values are obtained using imaging gradients and bipolar gradients with amplitudes up to 5 G/cm, the largest amplitude possible for our MR system, while keeping the timing the same.

By applying the bipolar gradient in different directions, the variance of the velocities in other directions can be measured. Moreover, equal amplitude bipolar gradients can be applied simultaneously along two orthogonal axes to

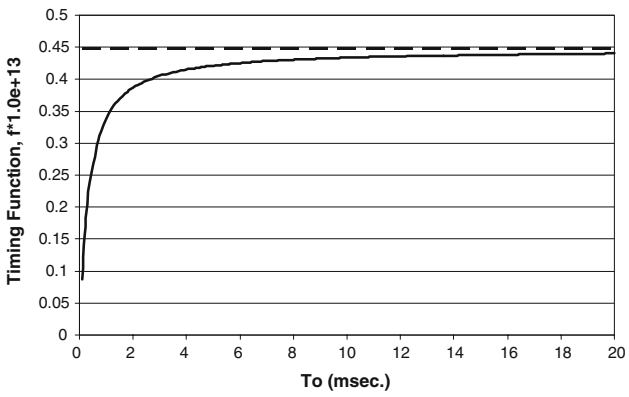

Fig. 2 *Solid curve*: the timing function $f(\tau, \mathrm{tr}, T_0) \times 10^{13}$ plotted against values of T_0 (ms) for the bipolar gradient timing used in this experiment. *Dashed line* the asymptotic value when $T_0 \gg \tau$

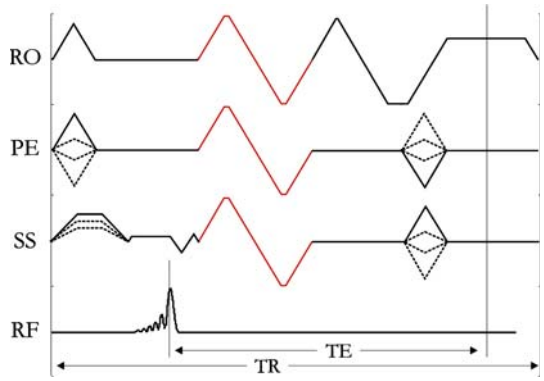

Fig. 3 The 3D, RF-spoiled, gradient echo MR sequence used to measure turbulent velocities. The *horizontal axis* is time (ms). The TR is the duration of the sequence, and the time between the formation of the transverse magnetization and the center of the echo is the TE. The logical axes of the sequence are the frequency encoding direction (labeled as "RO"), the in-plane phase encoding direction (labeled as "PE"), and the slice direction (labeled as "SS"). These *vertical axes* represent gradient amplitude (mT/m). The *dotted lines* indicate the phase encoding gradients that change from TR to TR in order to spatially encode the spin locations in the phase encode and slice directions. The magnitude of the excitation pulse is shown on the RF axis. The turbulence encoding is done with a bipolar pair of gradients (shown in *red*). The turbulence encoding gradients can be played out on a single axis, or on multiple axes as shown above

measure the velocity variance along the bisecting axis. This result can be combined with single axis results to calculate turbulent shear. For instance, $\sigma^2_{u+v} \equiv \left\langle (u'+v')^2/2 \right\rangle$, the variance of the velocity along the axis bisecting the streamwise (u') and cross stream (v') axes is measured by applying bipolar gradients simultaneously in the streamwise and cross stream directions. If bipolar gradients with amplitude G are applied simultaneously along the u' and v' axes, the resulting bipolar gradient along the bisecting axis has amplitude $\sqrt{2}G$. In this case, Eq. 5 becomes

$$\sigma^2_{u+v} = \left\langle (u'+v')^2/2 \right\rangle = \frac{\ln(S_0/S)}{\gamma^2 2G^2 f(\tau, \mathrm{tr}, T_0)} \tag{6}$$

The variance term can be expanded to

$$\left\langle (u'+v')^2/2 \right\rangle = \langle u'^2 \rangle/2 + \langle u'v' \rangle + \langle v'^2 \rangle/2.$$

Combining the measured velocity variance σ^2_{u+v} with values for σ^2_u and σ^2_v obtained by applying a single bipolar gradient in the streamwise and cross stream directions, respectively, the turbulent shear $\langle u'v' \rangle$ can be calculated from the formula $\langle u'v' \rangle = (\sigma^2_{u+v} - \sigma^2_u/2 - \sigma^2_v/2)$.

This technique for measuring velocity variance relies on the dephasing of the spin signals coming from the turbulent regions of the flow. The turbulence causes a signal change in a measurement volume through both intravoxel dephasing and ghosting artifacts. The ghosting artifacts occur because the randomness of the turbulence produces a change in the velocity distribution within a voxel from measurement to measurement made during one imaging TR. Because these signal changes are not consistent throughout the scan, the modulation of the k-space data will disperse signal from one voxel to other image voxels in the phase encoded direction. The extent of the effect can be measured by looking at the signal magnitudes in the regions outside of the flow channel in the MR images. Ghosting artifacts and other signal to noise issues contribute largely to the uncertainty of the measurements of the velocity standard deviation, σ_u. This uncertainty, $\mathrm{d}\sigma_u$, can be estimated by using the equation,

$$\mathrm{d}\sigma_u = \frac{\sqrt{\left(\frac{\mathrm{d}S_0}{S_0}\right)^2 + \left(\frac{\mathrm{d}S}{S}\right)^2}}{2\sigma_u G^2 f(\tau, \mathrm{tr}, T_0)} \tag{7}$$

where $\mathrm{d}S_0$ is an estimate of the uncertainty in S_0 and measured as the signal magnitude outside of the flow channel in the $G = 0$ image, and $\mathrm{d}S$ is an estimate of the uncertainty in S and measured as the signal magnitude outside of the flow channel in a $G > 0$ image. The equation shows that the uncertainty increases as the standard deviation of velocity decreases, but the increase is generally insignificant since large uncertainties in small values of σ_u are acceptable. More importantly, the equation also predicts that the uncertainty increases when the turbulence levels rise due to the increased ghosting signal and the decreased overall signal. In choosing the optimal bipolar gradient amplitudes, it is important to minimize this effect while creating enough signal reduction to accurately measure the velocity variance. Typically, a magnitude reduction of $\sim$50% works well.

The turbulence measurements were made using a 3D, RF-spoiled, gradient echo MR sequence as shown in Fig. 3. The turbulence encoding was done with a bipolar pair of gradients (shown in red) that could be played out along any combination of axes. The gradients were designed by specifying the maximal gradient area for each lobe. This value, which was typically on the order of 20 mT ms/cm, was chosen to produce significant dephasing in the turbulent flow downstream of the step but generally depends on the type of flow being imaged. The gradient waveforms were constructed using the minimum rise time and maximum gradient amplitude of the system in order to minimize their total duration. Further experiments could then be performed with smaller gradient areas by reducing the amplitudes of the turbulent encoding gradients. This allowed the timing of the gradient waveforms to remain unchanged from one experiment to the next. The amplitudes of the turbulent encoding gradients used in this experiment were G = 0, 2.5, 3.75, and 5 G/cm.

First order moment, $M_1 \equiv \int_0^\tau t' G(t') \mathrm{d}t'$, compensation was used to design readout and slice-select gradients with zero first moments (Haacke and Lenz 1987). This was done

to minimize the dephasing effects from these imaging gradients. Flow compensation was not done for the in-plane phase encode gradients, nor for the slice direction phase encoding gradients. The M_1 contributions from these gradients are very small at the center of k-space where most of the image information is collected. While the M_1 contributions are larger at the edges of k-space, these data produce minimal effects on the results. Displacement artifacts (Nishimura et al. 1991) were minimized by placing both the slice and in-plane phase encoding gradients as close as possible to the start of the read out gradient.

All experiments were performed on a 1.5-T MR system (GE Signa CV/I, $G_{max} = 50$ mT/m, rise time = 268 μs), with a single channel, extremity receive coil. Data were collected with a coronal slab chosen so that the field-of-view (FOV) was 28 cm in the streamwise and cross stream directions, and 60 1-mm-thick slices were prescribed to cover the extent of the flow channel in the spanwise direction. The in-plane matrix resolution was chosen to be 256 × 256 pixels, and a 0.3 fractional FOV in the phase encoding direction was used since the geometry is narrow in this direction. Other scan parameters included a flip angle of 25° and a receiver bandwidth of ±125 kHz. The resulting sequence repetition time (TR) and echo time (TE) were 5.0 and 3.7 ms, respectively. The time separating the centers of the bipolar gradient lobes is $\Delta = 740$ μs. A single scan of the complete geometry [matrix size 256 × (0.3 × 256) × 60] was acquired in 27 s.

A large number of signal acquisitions (NSA) was prescribed to increase the signal-to-noise ratio (SNR) of the data, and for each acquisition, a complete set of 3D data in k-space was taken before the next was begun. In this way, the temporal spacing between acquisitions of a given k-space position was the scan time of a single dataset. An NSA of 25 was prescribed, and the total scan time for one bipolar gradient amplitude in one direction was 11.5 min.

In addition to measuring the turbulent velocity variance, the full 3D mean velocity field was measured using the phase-contrast MRV method described in Elkins et al. (2003), modified to scan without the cine MRI functionality. The measurements were performed on the same 1.5 Tesla system, and we employed a single channel receive coil designed for human heads. The measurement domain contained the entire flow channel starting upstream of the converging flow before the step and extending eight step heights downstream. This 3D volume was scanned with a slab thickness of 64 mm, a FOV of 30 cm in the frequency direction, and a 0.5 fractional FOV of 15 cm in the phase encode direction. The imaging matrix was 64 × 256 × 256 which gave a voxel resolution of 1.0 mm × 1.2 mm × 1.2 mm. The scan timing parameters were TE = 2.0 ms, TR = 4.9 ms. The velocity encoding factor, Venc, was 225 cm/s in the streamwise direction and 75 cm/s in the cross stream and spanwise directions. One 3D scan was completed in 2 min 40 s. The flow domain was scanned 12 times, and the data were averaged.

2.2 Backward facing step steady flow loop

Both the MRV and PIV experiments used the same steady flow loop and test section. A centrifugal pump (Little Giant model no. TE-6MD-HC) circulated water at a flow rate of 77 ± 3 L/min. Gadolinium-based contrast agent (Omniscan, Nycomed, Inc.) was added to the water in a concentration of 0.5%. The volumetric flow rate was measured using a paddle wheel flow meter with an estimated uncertainty of 4%. MRV places a few restrictions on the experimental setup due to the large magnetic field and the sensitivity to RF noise. The pump was placed approximately 3 m from the magnet, and no other metallic parts were used in the loop. The Little Giant pump was tested for RF interference and was found to produce a negligible amount of noise in MR images.

Flow was supplied through approximately 3 m of 2.54 cm ID flexible tubing connected to a 2.4 m long by 5.1 cm i.d. development pipe which mated to the upstream end of the test channel. The 5.1 cm square test section was 65 cm long and was made from MRV and PIV compatible clear acrylic. It had a 28-cm-long development section with two 33% open area grids placed approximately 10 and 20 cm from the entrance. The backward facing step was created using a quarter of an acrylic tube with an outer radius of 3.2 cm mounted to one wall of the channel. The open backward facing part of the tube was closed by attaching an acrylic plate 1.6 mm thick. The test section exit which is 10 step heights downstream of separation is a 2.54 cm diameter hole connected to 6 m of 2.54 cm ID flexible tubing which runs out the back side of the magnet bore and is connected to a large water reservoir.

2.3 PIV system

PIV data were acquired on the flow centerplane using a conventional 2D DPIV system. The flow field was illuminated with two Continuum Minilite Nd:YAG lasers with 15 mJ/pulse at 532 nm and 10 Hz repetition rate. Standard optical components were used to combine the beams and form a light sheet approximately 400 μm thick and 57 mm wide at the waist. Images of flow tracers (9–13 μm diameter hollow glass spheres) were captured with a Kodak ES1.0 8-bit digital camera with a 1,018 × 1,008 pixel array, a 60% fill factor, and a pixel size of 9 μm. An 85 mm Micro-Nikkor lens with an aperture setting of 5.6 was used to achieve a FOV 5.6 cm × 5.6 cm which covered the entire height of the channel and 1.75 step heights in the streamwise direction. Measurements were taken at

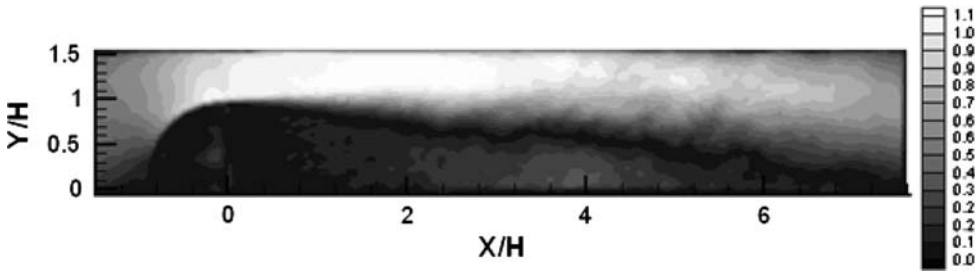

Fig. 4 2D cross section showing contours of the mean velocity magnitude normalized by U_{step} in the centerplane of the channel

three locations with the FOV centered at 1.3, 3, and 4.7 step heights downstream of the step.

The PIV image pairs were processed using the iterative 2D cross-correlation method developed by Westerweel (1997). The actual processing used a modified version of the code written by Han (2001). Each interrogation region (IR) consisted of 32 × 32 pixels thus giving a spatial resolution of 1.8 mm. With 50% overlapping IRs, a 62 × 62 velocity vector grid with a spacing of 0.9 mm was produced for each set of images. At each measurement location, 192 image pairs were used to calculate the turbulent flow statistics.

Uncertainty in magnification is estimated to produce uncertainty of 0.1% of the local flow velocity, while uncertainties related to calibration of the PIV system (calibration grid with respect to light sheet, angle of light sheet relative to flow direction, grid and camera) is estimated to ±0.5 pixels. Processing 192 image pairs gave a statistical uncertainty estimate of less than 1% for the local mean velocities and less than 8% for the local standard deviations.

3 Results

All of the results presented are for flow with a Reynolds number equal to 48,000 based on the step height H, 3.2 cm, and the mean bulk velocity at the edge of the step U_{step}, 1.4 m/s. Figure 4 shows a contour plot of the mean velocity magnitude measured in the centerplane using MRV. Velocities are normalized by U_{step}. The volumetric flow rates calculated from the MRV data agree to within ±4% of the flow meter reading. Figure 5 compares MRV and PIV normalized mean velocity vectors in a small region of the centerplane shown in Fig. 4. The agreement between the MRV and PIV is excellent across the entire cross section of the channel and within the ±10% estimated uncertainty in the MRV measurements (Elkins et al. 2004).

Spatial misregistration or displacement errors occur in the velocity data as the magnetized nuclei move during the measurement time TE. Since TE was 2.0 ms for the mean flow scans, the displacement is less than three voxel lengths

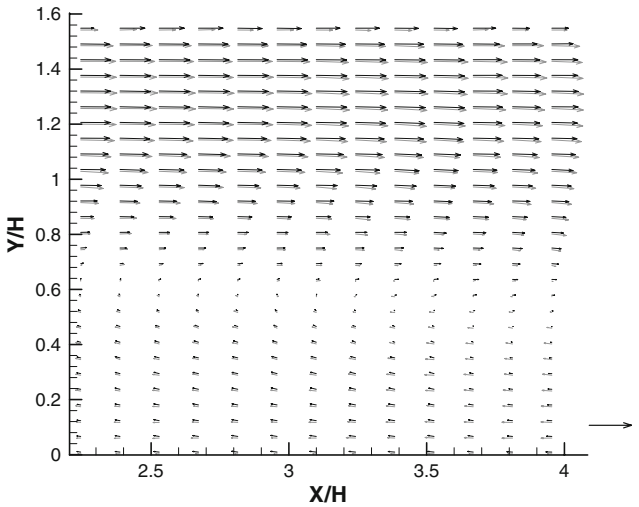

Fig. 5 Point by point comparison between MRV and PIV normalized velocity vectors in a small region in the centerplane of the channel (*black*-MRV, *gray*-PIV). Reference vector in lower right represents $\overline{U}/U_{step} = 1.0$

even for the fastest fluid particles which are found in the high speed, low turbulence potential core where the velocity is as high as 1.6 m/s.

There are spatial misregistration errors in the measurements of turbulent velocity variance as well. The motion of the fluid throughout most of the shear layer and recirculation region is slow, so the amount of motion during TE = 3.7 ms is limited to <1 voxel length. The motion in the high speed potential core is larger, but the fluctuations and the gradients of the fluctuations are small. Therefore, the overall errors in velocity variance created by the displacement during TE are small.

Figure 6 illustrates the concept behind the velocity variance measurement technique. Four images from the centerplane of the flow are shown from scans with the bipolar gradient applied in the streamwise direction. As the gradient strength increases from image a–d, the regions of the flow with the largest turbulent velocity variance become darker indicating lower signal strength due to the turbulent dephasing of the signal. This is most obvious in the shear layer since it contains the largest turbulent velocity fluctuations. Ghosting artifacts are evident in these images in the bands on either side of the flow channel. The

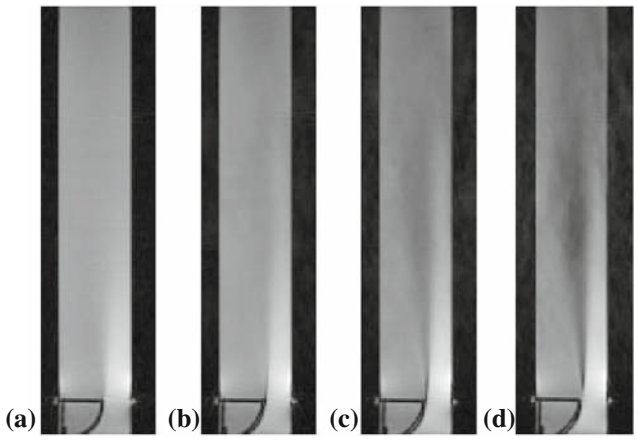

Fig. 6 Magnitude images in the centerplane of the flow with **a** $G = 0$ G/cm, **b** $G = 2.5$ G/cm, **c** $G = 3.75$ G/cm, and **d** $G = 5$ G/cm

ghosting signal increases with gradient amplitude. Note that the ghosting occurs to the side of the channel in areas of turbulent flow. In the less turbulent converging flow before the step, the ghosting artifacts are weak.

The rate of signal decay with increasing G^2 is found from a least squares fit of $\ln(S_0/S)$ versus G^2 for each measurement voxel. Figure 7 shows typical data for two points in the centerplane of the flow, ($x/H = 4.4$, $y/H = 0.25$) exemplary of a low turbulence level and ($x/H = 4.4$, $y/H = 0.7$) in a high turbulence region. The velocity variance at each point is found using Eqs. 4 and 5 with the slope of the least squares fit. The asymptotic value for $f(\tau, \text{tr}, T_0)$ at large T_0 is used over the entire flow field since T_0 is not known. This creates errors in regions with short T_0 and is addressed in Sect. 4.

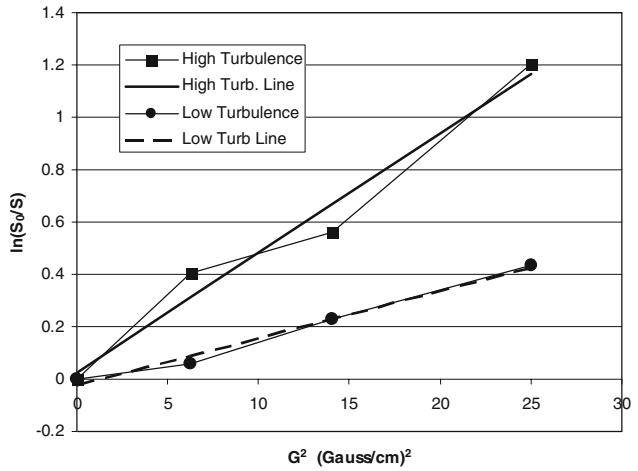

Fig. 7 Plots of the values for $\ln(S_0/S)$ versus G^2 and the least squares lines fit to these data at two points in the centerplane of the flow, ($x/H = 4.4$, $y/H = 0.25$) exemplary of a low turbulence level and ($x/H = 4.4$, $y/H = 0.7$) in a high turbulence region

Figures 8, 9, and 10 show contour plots of MRV and PIV values for σ_u/U_{step}, σ_v/U_{step}, and $-\langle u'v'\rangle/U_{\text{step}}^2$, respectively, in the centerplane of the flow. Here, σ_v is the standard deviation of the velocity in the cross stream, y, direction. Even though 25 dataset acquisitions were averaged to produce reasonably smooth images, additional smoothing of the MRV data was done by averaging each data point with the values of its six neighboring points in the 3D domain. There is good agreement between the contour levels and patterns for the MRV and PIV for both σ_u/U_{step} and σ_v/U_{step}, particularly in regions greater than 2–3 step heights downstream of the step where the integral time scale is large and the asymptotic value for $f(\tau, \text{tr}, T_0)$ applies.

The MRV measurements of $-\langle u'v'\rangle/U_{\text{step}}^2$ are quite noisy and do not agree well with the PIV measurements. These measurements have high uncertainty since the method to calculate $-\langle u'v'\rangle/U_{\text{step}}^2$ requires the subtraction of two single axis measurements from the measurement made with gradients applied simultaneously along two axes. However, the peak values in the separated shear layer show reasonable agreement indicating that the MRV technique provides useful estimates for the levels of turbulent shear.

Plots of the cross stream profiles for σ_u/U_{step}, σ_v/U_{step}, and $-\langle u'v'\rangle/U_{\text{step}}^2$ are shown in Figs. 11 and 12 for the downstream positions of $x/H = 4.4$ and 1.0, respectively.

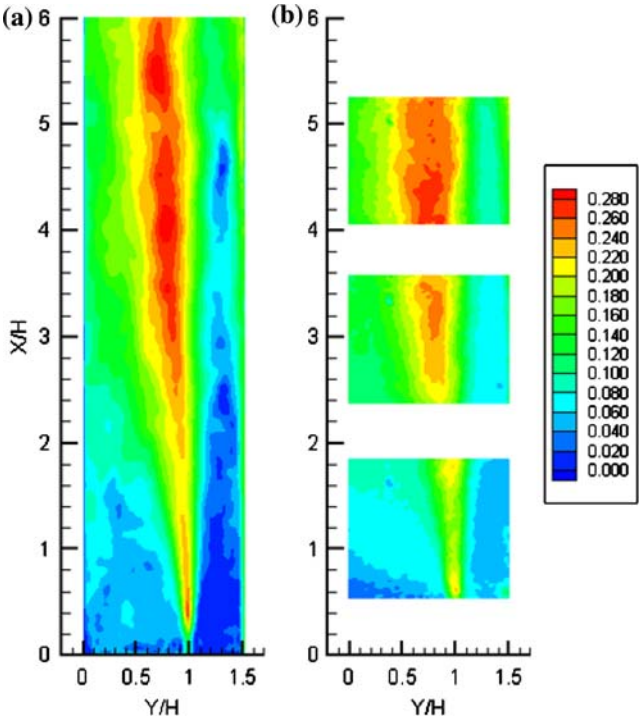

Fig. 8 **a** Contour plot of normalized streamwise velocity standard deviation, σ_u/U_{step}, measured with MRV. **b** Contour plot of normalized streamwise velocity standard deviation measured with PIV

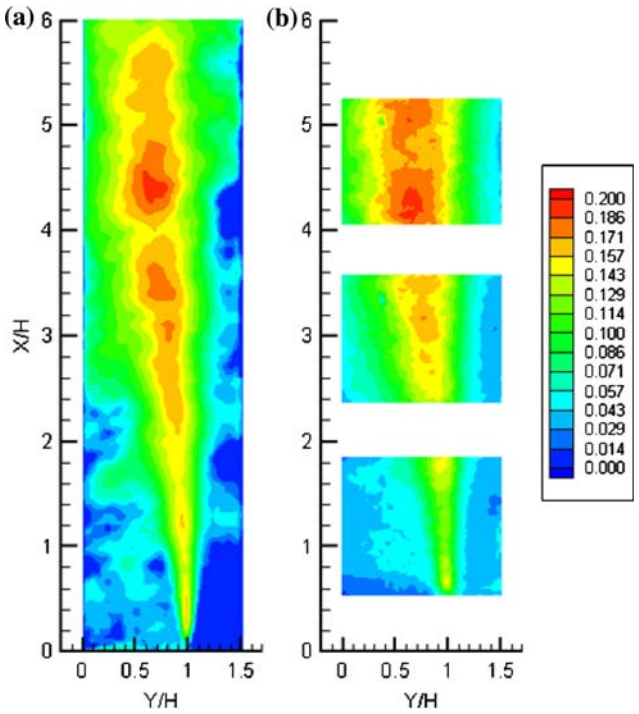

Fig. 9 **a** Contour plot of normalized cross stream velocity standard deviation, σ_v/U_{step}, measured with MRV. **b** Contour plot of normalized cross stream velocity standard deviation measured with PIV

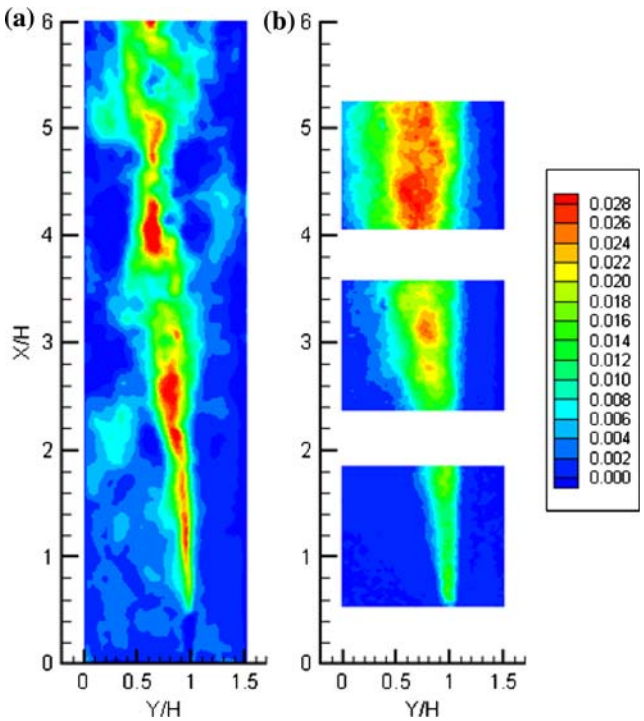

Fig. 10 **a** Contour plot of normalized turbulent shear, $-\langle u'v'\rangle/U^2_{\text{step}}$, measured with MRV. **b** Contour plot of normalized turbulent shear measured with PIV

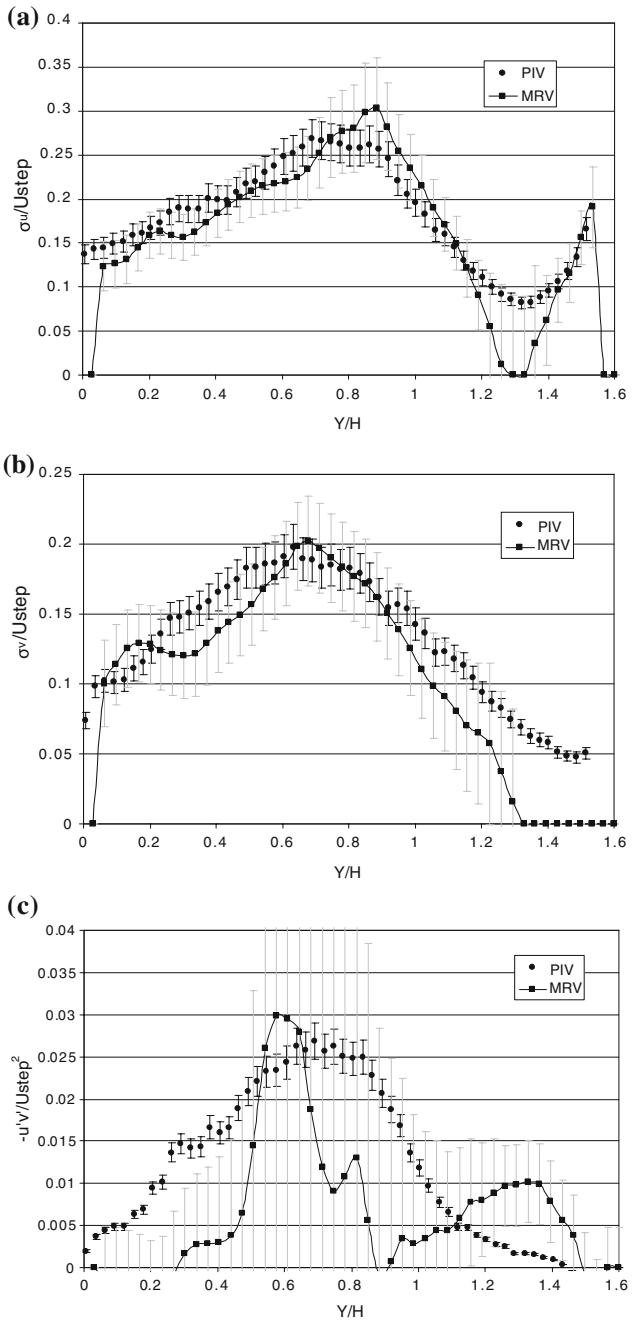

Fig. 11 MRV and PIV cross stream profiles of **a** σ_u/U_{step}, **b** σ_v/U_{step}, and **c** $-\langle u'v'\rangle/U^2_{step}$ at $X/H = 4.4$. *Error bars* indicate estimated local uncertainty at 95% confidence

Note that the values for σ_u/U_{step} and σ_v/U_{step} match to within the uncertainty estimates. The minimum uncertainty in the MRV curves is approximately 20% which is an estimate for the best performance one can expect from the current method.

In Fig. 11, both the MRV and PIV curves capture the displacement of the peak in the σ_u/U_{step} and σ_v/U_{step} profiles from $y/H = 1$, the height at which the shear layer

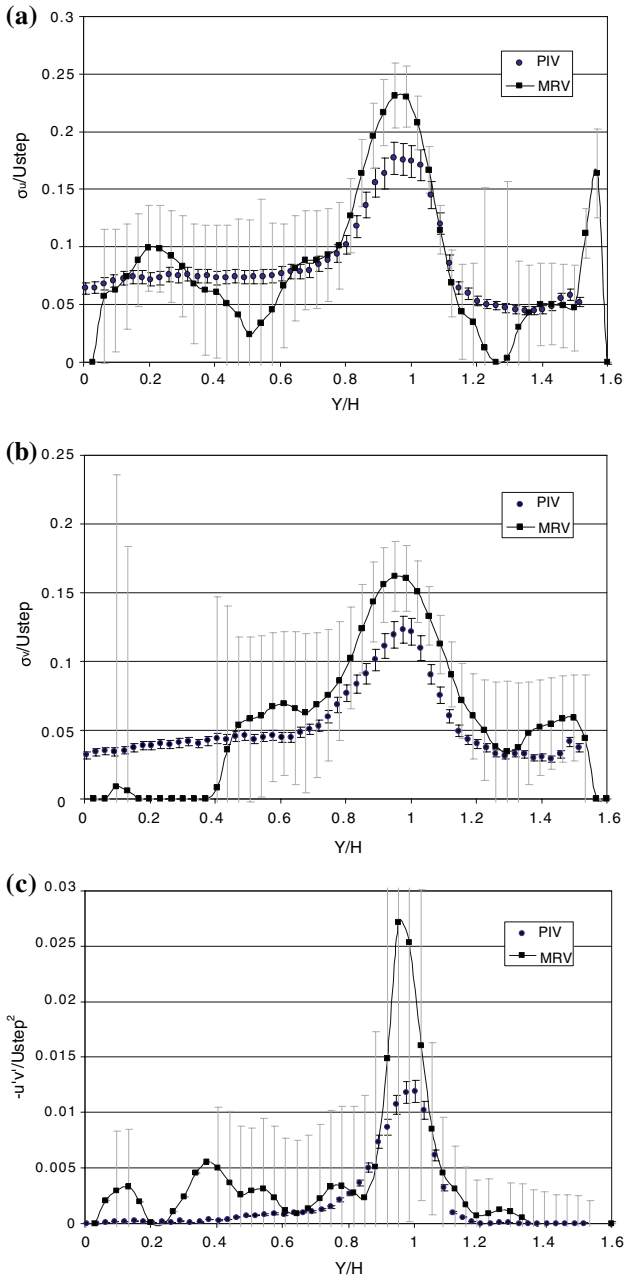

Fig. 12 MRV and PIV cross stream profiles of **a** σ_u/U_{step}, **b** σ_v/U_{step}, and **c** $-\langle u'v'\rangle/U_{step}^2$ at $X/H = 1$. *Error bars* indicate estimated local uncertainty at 95% confidence

originates. Both curves agree in the recirculation and shear layer regions for $y/H < 1.1$. However, the values for σ_u/U_{step} and σ_v/U_{step} in what remains of the freestream, $y/H = 1.1$–1.5, are underpredicted by the MRV, and some MRV measured values are zero. This is related to the weak turbulence in this region. Here the decrease in signal due to turbulent dephasing is small and similar to the signal level from ghosting artifacts combined with the background image noise making it difficult to measure a change in signal with gradient amplitude.

The agreement for the values of $-\langle u'v'\rangle/U_{step}^2$ is relatively poor except for the peak value. However, considering the large uncertainty associated with the MRV measurements, the MRV values are in range of the PIV values.

Figure 12 shows profiles one step height downstream of the step. The positions of the peak turbulent velocities and shear are captured by the MRV measurements, and there is good agreement across most of the flow except in the center of the shear layer. Here, the peak values are 20–30% too high for the standard deviations and slightly out of the uncertainty range. The error is even larger for the shear. Potential sources for this disagreement will be discussed below. Error bars are missing where the uncertainty could not be calculated because the MRV turbulence measurements are zero.

4 Discussion

The present technique provides a way to visualize turbulent flows (as seen in Fig. 6d), and if applied correctly, it can provide accurate measurements of velocity variance. The current results show that the derived equation to predict MR signal loss in turbulent flow works well several step heights downstream of the step but is less accurate in the regions closer to the step. In order to achieve the best accuracy, one must consider several factors: characteristics of the turbulence including turbulent time scales and diffusion lengths, sequence parameters including gradient amplitude and timing (τ, tr, and TE), and measurement volume and resolution.

One potential source of error is the use of the asymptotic value for the timing function, $f(\tau, \text{tr}, T_0)$. Essentially, this assumes that the Lagrangian integral time scale, T_0, is much longer than the duration of the bipolar gradient, $2\tau = 1.5$ ms. First, as is shown in Fig. 2, this is not a bad assumption if T_0 is greater than 3 ms, and it simplifies the analysis since T_0 is unknown and difficult to measure. The validity of the assumption can be checked by estimating the integral time scales for the different regions of the flow using characteristic length scales and velocity scales. For instance, at $x/H = 4.4$, the shear layer is $\sim$1.5 cm wide which roughly corresponds to the size of the large eddies in the flow. Two velocity scales are available: (1) the eddy advection velocity, which is $\sim$0.7 m/s and is measured using phase-contrast MRI, or (2) the predicted standard deviation of the velocity, σ_u, which is $\sim$0.38 m/s. The estimated time scales are 21 and 39 ms, respectively, and both are much larger than 3 ms.

In a region closer to the step, around $x/H = 1$, where the MRV measurements have more error, the shear layer width is $\sim$0.5 cm, the advection velocity is $\sim$0.7 m/s, and the

measured σ_u is $\sim$0.3 m/s. The estimated time scales are 7 and 16 ms, respectively. Here, too, both estimates are larger than 3 ms, and it seems unlikely that using the asymptotic value for $f(\tau, \mathrm{tr}, T_0)$ is responsible for the large errors.

Since we have PIV measurements of the mean velocities and turbulent statistics, we can calculate additional estimates of the integral time scales using calculations of the Taylor microscales and noting that the integral length scales are typically several times larger in moderate to high Reynolds number flows. If we assume the shear layer is steady and homogeneous with $\overline{U}$ changing only in the y direction, the rate of production of turbulent kinetic energy approximately equals the rate of energy dissipation (Tennekes and Lumley 1972). In addition, we assume the small scales of the turbulence are isotropic. While this is not strictly correct in the shear layer, it is a reasonable assumption to use for estimating the Taylor microscale. The following relationship can be used to calculate λ, the Taylor microscale,

$$\text{Production} = -\overline{u'v'}\frac{\mathrm{d}\bar{U}}{\mathrm{d}y} = \text{Dissipation} = \frac{15\nu\sigma_u^2}{\lambda^2} \tag{8}$$

Calculated from the PIV data, λ is 0.4 mm and 1.0 mm at $x/H = 1$ and $x/H = 4.4$, respectively. Using σ_u as the velocity scale gives time scales of 1.8 and 2.6 ms, respectively. Again, since the integral scales are much larger than those associated with the Taylor microscale, using the value for the timing function at large T_0 seems justified.

In many MRV applications, it is possible to scale the flow model and flow rates such that there are long integral time scales in the flow. In these cases, the asymptotic value for $f(\tau, \mathrm{tr}, T_0)$ applies if short but strong bipolar gradients are used. For instance, we scale most of the flow models so that the smallest features are on the order of millimeters and the velocity scales are on the order of 1 m/s. With these scaled models, the flow features are easily resolved, and the asymptotic value for $f(\tau, \mathrm{tr}, T_0)$ can be used without having to know the integral time scales.

In cases with shorter integral time scales, it is important to use appropriate values for T_0 to calculate $f(\tau, \mathrm{tr}, T_0)$ as pointed out by Kuethe and Gao (1995). In these cases, it might be possible to calculate integral time scales from measurements of the displacement autocorrelation function described in Stepisnik and Callaghan (2000) and Lasic et al. (2006). Alternatively, the method of Gatenby and Gore (1994) could be used to measure both $\sigma_u/U_{\mathrm{step}}$ and T_0 distributions. They used a method based on fractional echo acquisitions to vary TE which caused different amounts of signal loss in 2D images of a flow. Analysis of these images yielded maps for the values of T_0 and σ_u. While our method relies on knowledge of, or assumptions about the integral time scales, it is 3D and the data processing is much simpler. The present results are based on full echo acquisitions which were used to maximize SNR, and the timing is sufficiently short to provide accurate measurements throughout most of the flow.

The formula for $f(\tau, \mathrm{tr}, T_0)$ is derived assuming homogeneous turbulence for the local measurement volume. This assumption works well several step heights downstream where the shear layer is large compared to voxel width. However, the flow inhomogeneity close to the step where the shear layer is only a few voxels wide likely contributes significantly to the errors observed in this part of the flow.

Another important assumption made in this and other derivations is that the turbulent diffusion coefficient is locally constant around the measurement location. This assumption is justifiable if the spatial gradients of the turbulent diffusion coefficient, D_t, are small. A relevant parameter to consider is the ratio between a length scale characterizing the variation of D_t and a diffusion length scale dependent on the measurement time. When this ratio is large, the turbulent dephasing of the magnetization signal comes from local diffusion related to the local value of the velocity variance. An appropriate length scale for the variation of D_t is the separated shear layer thickness. The measurement diffusion length scale can be estimated as $\mathrm{TE} \cdot \sigma_u$. Considering a typical point in the separated shear layer, the shear layer thickness is around 1 cm, and the measurement diffusion length scale is less than 0.1 cm. The ratio of these two length scales is large, so our method should be valid throughout most of the flow except in the thin developing shear layer where the ratio can approach values close to 1. This, too, helps explain the disagreement between the PIV and MRV results seen in the developing shear layer at $x/H = 1$ in Fig. 12 and in the contour plots in Figs. 8 and 9 for $x/H < 2$.

One of the shortcomings of the MRV turbulence technique is that it has poor dynamic range. When there is a wide range of turbulent velocity variances in a flow, it is difficult to capture the high turbulence levels while resolving the low turbulence levels. As the images in Fig. 6 show, large gradient amplitudes can be used to create large signal ratios in order to resolve the weaker turbulent velocities. This creates very low signal magnitude where the turbulence is high. Large values for G also create bigger ghosting artifacts. The equation for the uncertainty (Eq. 7) tells us that large errors come from the combination of low signal magnitude S and large signal uncertainty $\mathrm{d}S$ to which the ghosting signals contribute. The best choice of G for any given flow is an important one; from experience, the best results occur when the signal loss is $\sim$50% of the $G = 0$ signal magnitude. A 50% signal loss balances the desire for a larger signal ratio to resolve the velocity variances and the need to reduce measurement uncertainty.

In many turbulent flows, there is a wide range of turbulent velocity variances that will be measured best with

multiple values for G. A least squares fit to the values for $\ln(S_0/S)$ and G^2 gives reasonable results for both high and low turbulent velocity variance with uncertainty as low as 20% as shown in Figs. 11 and 12. The uncertainty could be reduced further if the method were refined by using the scan data for the values of G estimated to give the best results. For example, the choice for which data to use could be based on an optimal value for S_0/S or a minimum acceptable estimated uncertainty.

Using lessons learned from this experiment, some guidelines can be presented that will help produce successful measurements in other flows. An appropriate spatial resolution should be chosen for the flow of interest. A resolution on the order of 1 mm is reasonably achievable with a 1.5T magnet, and is better than one needs in many cases. The signal to noise ratio depends on the cube of the nominal voxel dimension, so a small compromise on image resolution can buy a large improvement in SNR. However, the voxel resolution should be small enough to reduce effects from velocity field inhomogeneity and gradients in the turbulent diffusion coefficient. To use the methods described in this paper with Eqs. 4 and 5, the experimental parameters such as flow rate, model size, and bipolar gradient timing should be chosen such that the turbulent integral time scales are sufficiently longer than the gradient duration in order to simplify the calculation of $f(\tau, \mathrm{tr}, T_0)$. However, Eq. 2 can be applied when the correlation times are much smaller, in which case an asymptotic relation for $\tau \gg T_0$ can be used, or similar to the gradient duration, in which case T_0 must be measured possibly with the methods of Gatenby and Gore (1994), Stepisnik and Callaghan (2000), or Lasic et al. (2006). Next, preliminary scans should be performed to assess the loss of signal strength as a function of the bipolar gradient strength. Based on these results, G should be chosen to produce signal losses ranging from 20 to 70%. If measurements will be done using only two scans, the nonzero value for G should be chosen to produce $\sim$50% signal loss. A large NSA should be averaged to reduce statistical uncertainty and produce smooth results. Even with a large number of repetitions, the total scan time for the current test section for one value of G was less than 12 min. Moreover, multiple scans with a range of values for G were used, and the whole experiment was finished in less than 2 h. An important implementation in our scanning sequence is that a complete set of 3D data in k-space was finished before the next acquisition was begun. This produces better averages of the large scale structures in the turbulence.

5 Conclusions

A method is described by which the turbulent velocity variances can be measured in the entire flow field in a complex 3D geometry using MRI techniques. The method can be used to measure velocity variance in three directions and provide estimates of the turbulent shear. Results are presented for the streamwise and cross stream velocity variances and the associated turbulent shear in a backward facing step flow in a square channel. The results compare well with PIV measurements in the same flow. Critical scanning parameters are described and guidelines for choosing them are given. This method complements PC-MRI methods for measuring the mean velocity field and allows the measurement of the entire turbulent velocity field in complex geometries in and around potentially opaque objects using water or other MR compatible fluids.

Acknowledgments Christopher J. Elkins and John Eaton were supported by a grant from General Electric Aircraft Engines as part of the GE-University Strategic Alliance and a grant from the National Science Foundation (NSF CTS-0432478). Marcus Alley was supported by the same NSF grant and a grant from the National Institutes of Health (P41 RR09784).

References

Caprihan A, Fukushima E (1990) Flow measurements by NMR. Phys Rep 198(4):195–235

De Gennes PG (1969) Theory of spin echoes in a turbulent field. Phys Lett A 29(1):20–21

Dyverfeldt P, Sigfridsson A, Kvitting JP, Ebbers T (2006) Quantification of intravoxel velocity standard deviation and turbulence intensity by generalizing phase-contrast MRI. Magn Reson Med 56(4):850–858

Elkins CJ, Markl M, Pelc N, Eaton JK (2003) 4D Magnetic resonance velocimetry for mean velocity measurements in complex turbulent flows. Exp Fluids 34(4):494–503

Elkins CJ, Markl M, Iyengar A, Wicker R, Eaton JK (2004) Full-field velocity and temperature measurements using magnetic resonance imaging in turbulent complex internal flows. Int J Heat Fluid Flow 25(5):702–710

Gao JH, Gore JO (1991) Turbulent flow effects on NMR imaging: measurement of turbulent intensity. Med Phys 18(5):1045–1051

Gatenby JC, Gore JC (1994) Mapping of turbulent intensity by magnetic resonance imaging. J Magn Reson B 104(2):119–126

Gatenby JC, Gore JC (1996) Echo-planar-imaging studies of turbulent flow. J Magn Reson A 121:193–200

Haacke EM, Lenz GW (1987) Improving MR image quality in the presence of motion by using rephasing gradients. AJR Am J Roentgenol 148(6):1251–1258

Han D (2001) Study of turbulent nonpremixed jet flames using simultaneous measurements of velocity and ch distribution. Stanford University, USA

Iaccarino G, Elkins C (2006) Towards rapid analysis of turbulent flows in complex internal passages. Flow Turbul Combust 77:27–39

Kuethe DO (1989) Measuring distributions of diffusivity in turbulent fluids with magnetic-resonance imaging. Phys Rev A 40(8): 4542–4551

Kuethe DO, Gao JH (1995) NMR signal loss from turbulence: models of time dependence compared with data. Phys Rev E 51(4): 3252–3262

Lasic S, Stepisnik J, Mohoric A (2006) Displacement power spectrum measurement by CPMG in constant gradient. J Mag Res 182: 208–214

Li TQ, Seymour JD, Powell RL, McCarthy KL, Odberg L, McCarthy MJ (1994) Turbulent pipe-flow studied by time-averaged NMR imaging—measurements of velocity profile and turbulent intensity. Magn Reson Imaging 12(6):923–934

Newling B, Poirier CC, Zhi Y, Rioux JA, Coristine AJ, Roach D, Balcom BJ (2004) Velocity imaging of highly turbulent gas flow. Phys Rev Lett 93(15):154503–154504

Nishimura DG, Jackson JI, Pauly JM (1991) On the nature and reduction of the displacement artifact in flow images. Magn Reson Med 22(2):481–492

Stepisnik J, Callaghan PT (2000) The long time tail of molecular velocity correlation in a confined fluid: observation by modulated gradient spin-echo NMR. Phys B 292:296–301

Tennekes H, Lumley JL (1972) A first course in turbulence. MIT Press, Cambridge

Westerweel J (1997) Fundamentals of digital particle image velocimetry. Meas Sci Technol 8(12):1379–1392